Science Bulletin 65 (2020) 1659–1666

Contents lists available at ScienceDirect

Science Bulletin

journal homepage: www.elsevier.com/locate/scib

Article

Trimethyltriazine-derived olefin-linked covalent organic framework with ultralong nanofibers

Fan Zhang [a], Shice Wei [a], Weiwei Wei [a], Jiang Zou [b], Guoying Gu [b], Dongqing Wu [a], Shuai Bi [a,*], Fan Zhang [a,c,*]

[a] School of Chemistry and Chemical Engineering, Shanghai Jiao Tong University, Shanghai 200240, China
[b] Robotics Institute, School of Mechanical Engineering, Shanghai Jiao Tong University, Shanghai 200240, China
[c] State Key Laboratory of Metal Matrix Composites, Shanghai Jiao Tong University, Shanghai 200240, China

A R T I C L E I N F O

Article history:
Received 12 March 2020
Received in revised form 12 May 2020
Accepted 26 May 2020
Available online 29 May 2020

Keywords:
Covalent organic framework
Olefin linkage
Nanofiber
Micro-supercapacitor
Energy storage

A B S T R A C T

Two-dimensional (2D) olefin-linked covalent organic frameworks (COFs) with excellent π-electron communication and high stability are emerging as promising crystalline polymeric materials. However, because of the limited species of COFs, their characteristics, processability and potential applications have not been completely understood and explored. In this work, we prepared two novel olefin-linked 2D COFs through Knoevenagel condensation of 2,4,6-trimethyl-1,3,5-triazine with tritopic triazine-cored aldehydes. The resulting COFs exhibit highly crystalline honeycomb-like structures stacked from hexagonal-latticed polymeric layers and display well-defined nanofibrillar morphologies with the uniform diameters of ca. 80 nm and ultra-lengths up to several micrometers. Such COF nanofibers can be readily composited with carbon nanotubes into high-quality continuous thin films, which are further compacted by a typical hot-pressing process to enhance their densities and mechanical strength without changing their fibrous microstructures. Such film-fabricated interdigital microelectrodes and the ionogel electrolyte are assembled into planar micro-supercapacitors (MSCs), which exhibit an outstanding areal capacitance of 44.3 mF cm^{-2}, large operating voltage window of 2.5 V, high volumetric energy density of 38.5 mWh cm^{-3} as well as excellent cycling stability.

1. Introduction

Recently, forming the olefin linkage (—C=C—) through facile-performed Knoevenagel/Aldol condensation is becoming a sustainable and reliable tool to expand the regimes of covalent organic frameworks (COFs) because of the utilization of the key monomers, such as 2,4,6-trimethyl-1,3,5-triazine, with low toxicity and generality [1–5]. Owing to a large number of monomers available for Knoevenagel/Aldol condensation polymerization, in principle, the geometric, electronic and topological structures of such olefin-linked COFs could be rationally designed and finely tailored [6–13]. Besides the outstanding stability, newly reported olefin-linked COFs also exhibit some unexpected promising characteristics, which are highly desirable for catalysis, sensing, energy conversion, etc. [2–5]. For example, Lyu et al. [2] reported an olefin-linked COF which enables loading strong boron-based Lewis acid for catalyzing Diels–Alder reaction. Acharjya et al. [3] found the [2 + 2] photo-cyclization of vinylene linkages between the adjacent COF layers. Jadhav et al. [4] manifested that the finely-tuned optical behaviors of such COFs via the modification of co-monomers. Our group revealed the semiconducting activities of the olefin-linked COFs for photocatalytic hydrogen and oxygen evolution, as well as energy storage [5,14–16].

On-chip planar micro-supercapacitors (MSCs) have become a promising power source for high-performance wearable and portable devices [17,18]. Materials such as graphene [19–22], carbon nanotube [23,24], Mxene [25–27], and MoS_2 [28,29] exhibit distinct merits as the electrodes of MSCs due to their excellent stability and electric conductivity. On the other hand, the formation of well-defined morphologies could helpfully deliver intrinsic characteristics and improve processability, but it is still full of challenges due to the lack of tailorable structures for those conventional materials. Interestingly, we found that incorporation of triazine units into the olefin-linked COFs promotes the formation of well-defined nanofibrillar morphologies, which are suitable for the fabrication of high-quality thin-film photoelectrodes or interdigital electrodes of MSCs [5,16]. With regard to these, we synthesized two new olefin-linked COFs via Knoevenagel condensation of 2,4,6-trimethyl-1,3,5-triazine and 1,3,5-tris-(4-formylphenyl)triazine or 1,3,5-tris-(4′-formyl-biphenyl-4-yl)triazine (Scheme 1).

* Corresponding authors.
E-mail addresses: bishuai-kiven@sjtu.edu.cn (S. Bi), fan-zhang@sjtu.edu.cn (F. Zhang).

https://doi.org/10.1016/j.scib.2020.05.033
2095-9273/

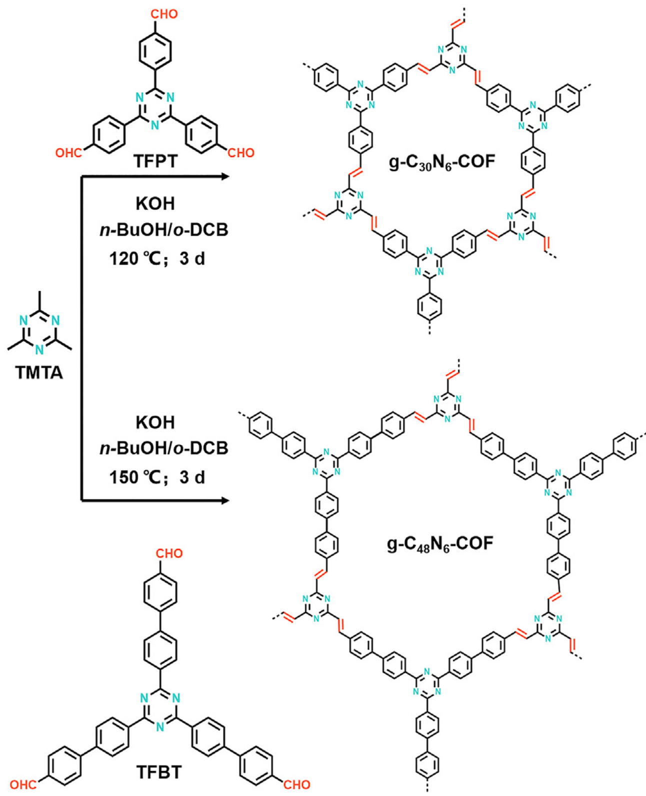

Scheme 1. (Color online) Synthetic routes to g-$C_{30}N_6$-COF and g-$C_{48}N_6$-COF.

The introduction of rich triazine units into the frameworks is mainly considered by the following: (1) the triazine ring without hydrogen atoms features a condensed planar structure, which is favorable for the formation of a high crystalline structure; (2) it enables π-electron conjugation on the three *meta*-positions for strengthening electric conductivity; (3) its rich pyridinyl nitrogen atoms create substantial active sites [30–37]. For the as-prepared COFs, their crystalline structures with high surface area and regular open nanochannels were fully characterized and considerably confirmed. Microstructural analyses clearly revealed the nano-fibrillar morphologies of COFs. When combined with carbon nanotubes (CNTs), these COF fibers exhibit excellent thin-film forming capability and outstanding mechanical processability. Eventually, the fabrication of these COFs into MSCs was systematically investigated, revealing high energy and power densities.

2. Materials and methods

2.1. Synthetic procedures of 2,4,6-tri((E)-styryl)-1,3,5-s-triazine (TST, model compound)

An oven-dried long-neck Schlenk flask was equipped with a magnetic stir bar and charged with 2,4,6-trimethyl-1,3,5-triazine (TMTA, 246 mg, 2.0 mmol), benzaldehyde (636.7 mg, 6 mmol), KOH (448.8 mg, 8 mmol) and 40 mL CH_3OH under the protection of N_2. Then the mixture was heated to 80 °C and stirred for 24 h under a N_2 atmosphere. After cooling down to room temperature, the crude product was extracted with dichloromethane and concentrated to obtain a pale yellow solid. The crude product was purified by recrystallization in a mixed solution of dichloromethane/methanol to afford the pure model compound as white solids. Yield: 90% (697.5 mg). ^1H NMR (400 MHz, CD_2Cl_2, δ): 8.31 (d, J = 12.8 Hz, 1H), 7.72 (d, J = 5.7 Hz, 2H), 7.46–7.41 (m, 3H), 7.18 (d, J = 12.8 Hz, 1H); ^{13}C NMR (100 MHz, CD_2Cl_2, δ): 171.48, 141.55, 135.75, 130.07, 129.12, 128.33, 126.60.

2.2. Synthesis of g-$C_{30}N_6$-COF

In an argon-filled glove box, TMTA (30.79 mg, 0.25 mmol), 1,3,5-tris(4-formylphenyl)triazine (TFPT, 98.35 mg, 0.25 mmol) and KOH (42.08 mg, 0.75 mmol) were dissolved in a mixed solvent containing 7 mL *n*-butanol and 3 mL *o*-dichlorobenzene and sealed in a thick-walled pressure tube. After ultrasonication for 5 min, the resulting pale-yellow solution was heated at 120 °C for a 3-day reaction. After cooling to room temperature, the precipitate was collected and washed with methanol, tetrahydrofuran, acetone and dichloromethane in sequence for three times (10 mL for each), and then dried under vacuum at 60 °C for 12 h. Finally, pure COF sample was afforded as pale-yellow powders (yield: 85%, relative to the used amount of monomer).

2.3. Synthesis of g-$C_{48}N_6$-COF

In an argon-filled glove box, TMTA (30.79 mg, 0.25 mmol), 1,3,5-tris-(4′-formyl-biphenyl-4-yl)triazine (TFBT, 155.42 mg, 0.25 mmol) and KOH (42.08 mg, 0.75 mmol) were dissolved in a binary solvent of 7 mL *n*-butanol and 3 mL *o*-dichlorobenzene and sealed in a thick-walled pressure tube. After ultrasonication for 5 min, this mixture was heated up to 150 °C for a 3-day reaction. The resulting precipitates were collected and thoroughly washed with methanol, tetrahydrofuran, acetone and dichloromethane in sequence for three times (10 mL for each), and then dried under vacuum at 60 °C for 12 h. The target COF sample was achieved as a green powder in a yield of approximately 80% relative to the used amount of monomer.

2.4. Preparation of COF/CNT hybrid thin film

g-$C_{30}N_6$-COF (g-$C_{48}N_6$-COF) and single-walled carbon nanotube (SWCNT) were suspended in two bottles with ethanol. The suspensions of COF and SWCNT were treated with ultrasonication for 1 h and overnight respectively. Then two bottles of uniform suspensions were mixed together. At last, the mixed suspension was vacuum-filtrated through a polypropylene (PP) membrane filter. The obtained thin film was carefully dried overnight under room temperature and directly separated from the PP membrane.

2.5. Preparation of ionogel electrolyte

Poly(vinylidene fluoride-co-hexafluoropropylene) (PVDF-HFP) was firstly dissolved in acetone. Then, 1-ethyl-3-methylimidazolium tetrafluoroborate ($EMIMBF_4$) was mixed with the above solution of PVDF-HFP/acetone and stirred magnetically for 12 h. The optimal mass ratio of $EMIMBF_4$ and PVDF-HFP was adjusted to be 3:1.

2.6. Preparation of COF/CNT micro-supercapacitor

The COF/CNT hybrid thin film was transferred to the substrate (polyethylene terephthalate, PET) and further processed to interdigital microelectrodes (width of 1.1 mm, length of 18 mm, and interspace of 0.4 mm) by using laser scribing. The resultant ionogel electrolyte of $EMIMBF_4$/PVDF-HFP was slowly drop-casted on the project area of electrode patterns and solidification overnight. Besides, Cu foil was adhered to the end of electrode by silver paste as a connector to fabricate COF-MSC.

2.7. Preparation of pure CNT-based micro-supercapacitor

SWCNT were suspended in ethanol and the suspension was treated with ultrasonication for overnight. The suspension was vacuum-filtrated through a PP membrane filter. The obtained thin film was transferred to the substrate (polyethylene terephthalate, PET) and further processed to interdigital microelectrodes (width of 1.5 mm, length of 18 mm, and interspace of 0.8 mm) by using laser scribing. The ionogel electrolyte of $EMIMBF_4$/PVDF-HFP was slowly drop-casted on the project area of electrode patterns and solidification overnight. Finally, Cu foil was adhered to the end of electrode by silver paste as a connector to fabricate pure CNT-based MSC.

3. Results

The target COFs (denoted as g-$C_{30}N_6$-COF and g-$C_{48}N_6$-COF) were synthesized under the optimized thermodynamic conditions through Knoevenagel condensation. In a typical g-$C_{30}N_6$-COF preparation procedure, TMTA, TFPT and KOH in a molar ratio of 1:1:3 were suspended in a binary solvent system of *n*-butanol and *o*-dichlorobenzene (v/v, 7/3) and sealed in a thick-walled pressure tube under an Ar atmosphere. After ultrasonication for 5 min, the mixture was heated up to 120 °C for 72 h, leading to the formation of precipitate at the bottom of the tube, which was filtered and washed with organic solvents, then dried at 60 °C for 12 h. Finally, the g-$C_{30}N_6$-COF sample was collected as pale-yellow powders in 85% yield (see the Supplementary materials for detailed procedures).

The crystalline frameworks of g-$C_{30}N_6$-COF and g-$C_{48}N_6$-COF were confirmed by powder X-ray diffraction (PXRD) analyses. The highly intense peaks at 2θ = 5.72° and 4.14° for g-$C_{30}N_6$-COF and g-$C_{48}N_6$-COF were reflected by their (1 0 0) planes, respectively. The well-resolved reflections of (1 1 0), (2 0 0), (2 1 0) and (0 0 1) planes at 2θ = 9.85°, 11.51°, 15.17° and 26.07° for g-$C_{30}N_6$-COF revealed its good crystallinity (Fig. 1a), comparable to the typical olefin-linked COF materials [2,7,9]. Meanwhile, for g-$C_{48}N_6$-COF, the distinguishable reflections of (1 1 0), (2 0 0), (2 1 0) and (0 0 1) planes at 2θ = 7.01°, 8.30°, 10.76° and 24.96° suggest its intrinsic long-range ordering (Fig. 1b). Crystal structure modelings manifested the simulated patterns of honeycomb hexagonal unit cells adopting eclipsed (AA) layer stacking modes matched well with the experimental patterns for the two COFs. Pawley refinement of predicted AA-stacking unit cell towards experimental PXRD patterns generated the refined PXRD profiles, unit cell parameters, profile differences and residual values for

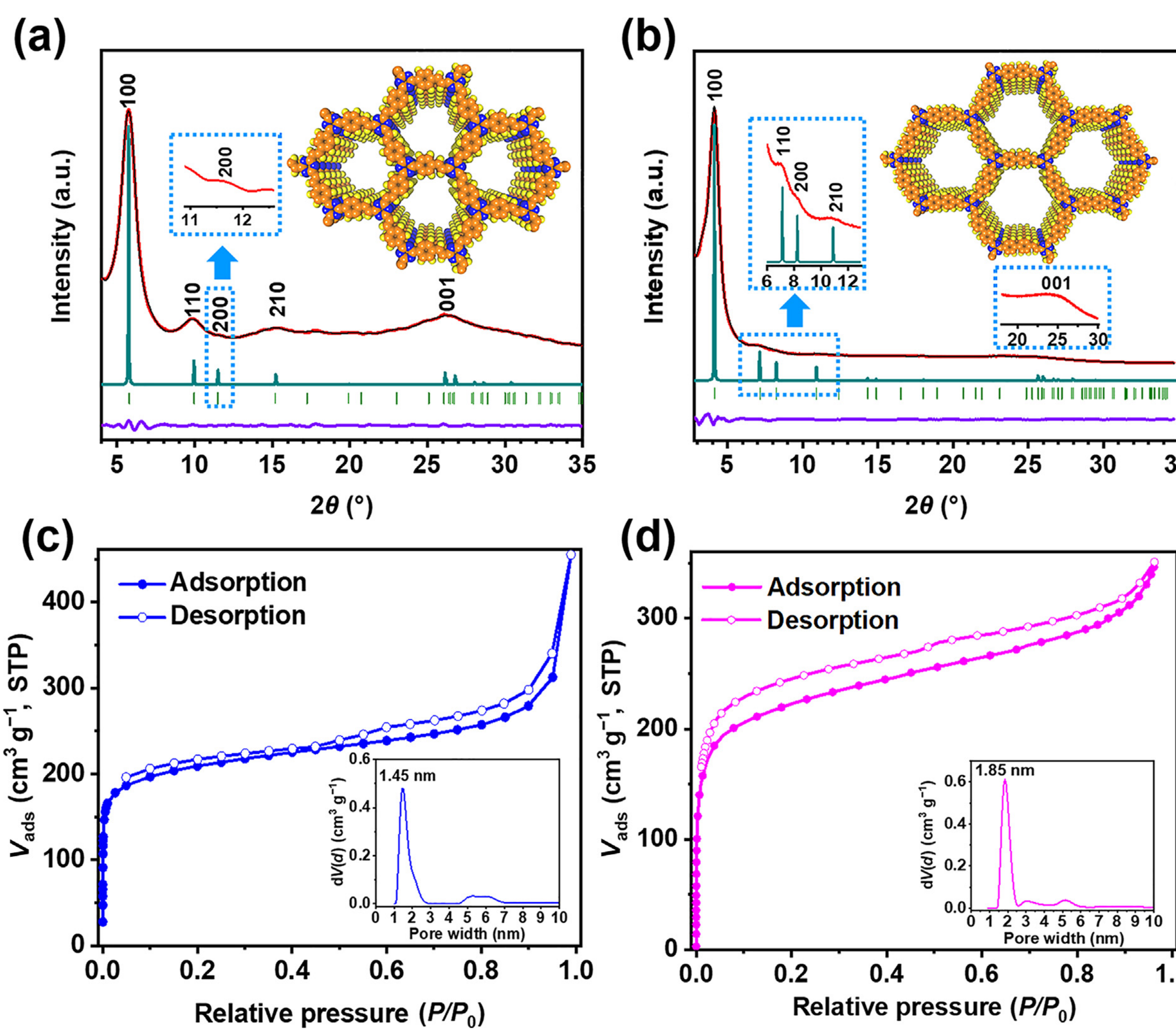

Fig. 1. (Color online) Characterizations of crystal and porous structures for COFs. (a) and (b) Experimental PXRD patterns (red) of g-$C_{30}N_6$-COF and g-$C_{48}N_6$-COF, along with Pawley refinement profiles (black), simulated profiles assuming eclipsed (AA) stacking mode (cyan), Bragg positions (green) and the refinement differences (violet). (c) and (d) Nitrogen sorption isotherms of g-$C_{30}N_6$-COF and g-$C_{48}N_6$-COF, inset shows the pore size distribution calculated by cylindrical quenched-solid density functional theory (QSDFT) equilibrium model.

g-$C_{30}N_6$-COF ($P\bar{6}$, $a = b = 17.763$ Å and $c = 3.406$ Å, $\alpha = \beta = 90°$, $\gamma = 120°$, $R_P = 2.44\%$; $R_{WP} = 3.08\%$) and g-$C_{48}N_6$-COF ($P\bar{6}$, $a = b = 24.765$ Å and $c = 3.471$ Å, $\alpha = \beta = 90°$, $\gamma = 120°$, $R_P = 1.73\%$; $R_{WP} = 2.17\%$).

The permanent porosities of g-$C_{30}N_6$-COF and g-$C_{48}N_6$-COF were analyzed by the N_2 sorption isotherms recorded at 77 K. Rapid N_2 uptakes at the relatively lower pressure range ($P/P_0 < 0.1$) suggest the typical type-I reversible isotherms of the two COFs with microporous structures (Fig. 1c and d). By employing the Brunauer–Emmett–Teller (BET) method towards the adsorption isotherms, the BET surface areas of g-$C_{30}N_6$-COF and g-$C_{48}N_6$-COF were calculated to be 784 and 830 $m^2\ g^{-1}$, respectively. In addition, cylindrical quenched-solid density functional theory (QSDFT) equilibrium model was used to calculate the pore-size distribution based on the adsorption isotherms, showing mono-dispersed pore diameters at 1.45 and 1.85 nm for g-$C_{30}N_6$-COF and g-$C_{48}N_6$-COF, respectively, well in line with their predicted pore size diameters from the Connolly surface of AA-stacking mode (Figs. S33 and S34 online).

Furthermore, in conjunction with the reference compound 2,4,6-tri((E)-styryl)-1,3,5-triazine (TST), the chemical structures of g-$C_{30}N_6$-COF and g-$C_{48}N_6$-COF were confirmed by Fourier transform infrared (FT-IR) and solid-state ^{13}C cross-polarization magic-angle spinning (CP-MAS) NMR spectroscopy. The FT-IR spectra of g-$C_{30}N_6$-COF and g-$C_{48}N_6$-COF were closely similar to that of the model compound TST (Fig. 2a). The resonance signals at 1633 and 980 cm^{-1} could be attributed to the stretching and bending vibrations of *trans*-olefin, respectively. The high-intensity peak at 1510 cm^{-1} corresponded to the triazine moiety. The disappearance of methyl (at 2930 cm^{-1}) and carbonyl (at ~1701 cm^{-1}) stretching vibrations suggested the considerably high-degree polymerization of the monomers (Fig. S10 online). In addition, the defined polymeric backbones of g-$C_{30}N_6$-COF and g-$C_{48}N_6$-COF were elucidated by comparing their ^{13}C NMR spectra with the reference molecule TST. The two well-resolved peaks at ca. 170 ppm were attributed to the carbons of triazine rings. The signal of phenylene attached triazine carbons shifted downfield ca. 7 ppm in comparison with that of the olefin attached triazine carbons, due to the more electron-donating character of phenylene. The strong and broad resonance signals at 120–140 ppm originated from the (poly-) phenylene and olefin carbons, which could be well distinguished according to the reference compound TST (Fig. 2b).

The microstructures of g-$C_{30}N_6$-COF and g-$C_{48}N_6$-COF were characterized by scanning electron microscopy (SEM) and transmission electron microscopy (TEM). The well-defined filamentous fibers with a diameter of ca. 80 nm and length of several micrometers were found in the SEM and TEM images of g-$C_{30}N_6$-COF (Fig. 3a and b). g-$C_{48}N_6$-COF showed similarly fibrillar morphology with lower surface smoothness and regularity than that of g-$C_{30}N_6$-COF (Figs. S4a and S6 online). In addition, the high-resolution TEM image of g-$C_{48}N_6$-COF (Fig. S7 online) revealed the presence of characteristic lattice fringes of (1 0 0) plane with the periodic distance of 1.8 nm which fits well to the pore dimensions determined from N_2 sorption analysis (1.85 nm), manifesting its intrinsic long-range ordered structure and further verifying the eclipsed AA-stacking arrangement between the two-dimensional (2D) COF layers. In order to understand the morphological evolution of the COF fibers, we performed a series of time-dependent experiments to synthesize g-$C_{30}N_6$-COF [38]. The microstructures of samples collected at different reaction time were analyzed by SEM measurement. For a 2-hour reaction, the SEM image of the sample showed irregular aggregates comprising short rods with rough surfaces (Fig. S8a online). After prolonging the polymerization time to 12, 24, and 48 h, respectively, the lengths, smoothness of surfaces, and uniformity of diameters of fiber-like samples gradually increased (Fig. S8b–d online). Further prolonging the reaction time, there was no obvious change in the morphology. Additionally, as illustrated in the XRD patterns of the samples at different reaction time (Fig. S9 online), the intensity of the (1 0 0) peaks gradually increased along with the extension of polymerization time, suggesting a gradual improvement of crystallinity. These phenomena indicate that the growth of the COF nanofibers is accompanied by the enhancement of the crystallinity. It is known that the triazine units in the 2D COFs helpfully promote the vertical stacking of the COF layers along the *Z*-axis because of the strong π–π interaction, leading to the enhancement of crystallinity and formation of rod-like or ribbon-shaped morphologies [30,39]. Therefore, in our case, we presume that the fibrous morphologies of the as-prepared COFs originate from the presence of planar triazine moieties at the knots of the COF layer. Substantial triazine moieties within these COFs seem to favorably offer a much stronger π–π stacking driving force for the rapid and efficient growth of 2D COF layers along one direction, thus tending to form much longer fibers, as compared to our previously reported olefin-linked COFs with fewer triazine moieties [5,16]. Interestingly, these COF fibers can be well-dispersed in some polar organic solvents (e.g., ethanol), allowing for convenient manipulation into thin films through vacuum filtration, but the resulting pure COF-based films only exhibit weak mechanical strength. Therefore, the composition of such COF nanofibers with fibrous CNTs was examined under

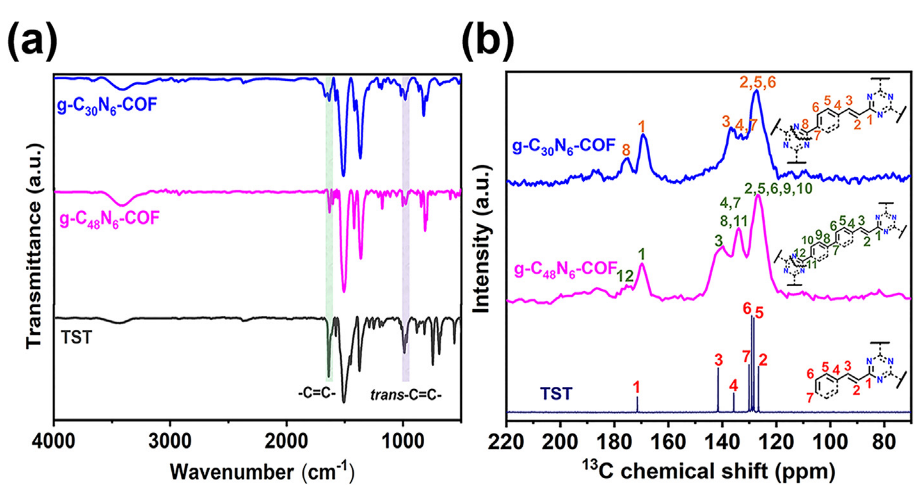

Fig. 2. (Color online) Characterizations of chemical structures for COFs and model compound. (a) FT-IR spectra of g-$C_{30}N_6$-COF, g-$C_{48}N_6$-COF and 2,4,6-tri((E)-styryl)-1,3,5-triazine (TST). (b) ^{13}C CP/MAS solid-state NMR spectra of g-$C_{30}N_6$-COF and g-$C_{48}N_6$-COF, compared with liquid ^{13}C NMR spectra of TST (model compound) in CD_2Cl_2.

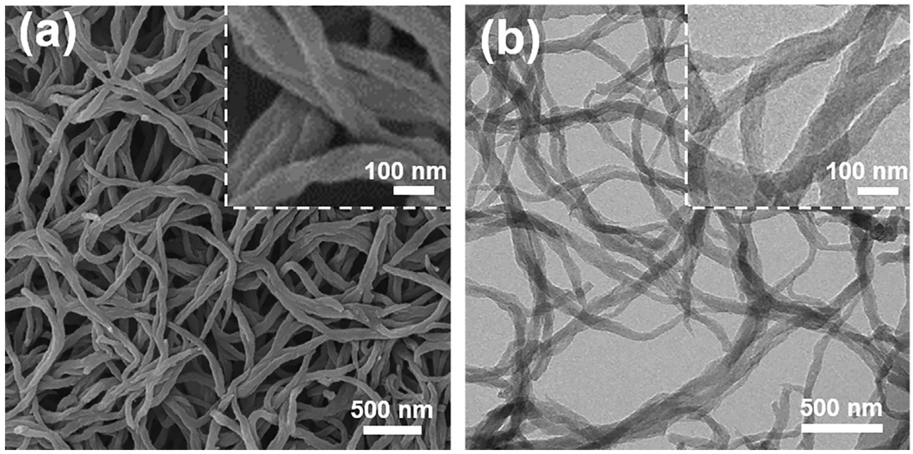

Fig. 3. (a) SEM and (b) TEM micrographs of g-$C_{30}N_6$-COF.

different mass ratios (from COF/CNT = 1/9 to 9/1, w/w) (Figs. 4a, S17 online). In a typical protocol, the g-$C_{30}N_6$-COF sample and CNT were suspended in ethanol in a mass ratio of 7/3 (w/w), then filtered through a vacuum filter, leading to the formation of a free-standing COF/CNT film composite with ca. 50 μm thickness (Fig. 4b). Its mechanical characterization showed good mechanical strength with a maximum stress of 1.5 MPa (Fig. S15 online) and excellent flexibility (stable under bending > 90° for at least 100 times). The thickness of this film was compacted from 50 to 10 μm without changes in its nano-scale fibrous microstructures through a typical hot-pressing treatment at 30-MPa pressure and 50 °C. Furthermore, the compacted film could withstand a maximum stress of 7.2 MPa, which is nearly five times the pressure of the pre-pressed film could withstand (Fig. 4c). These consequences revealed that such olefin-linked COFs could undergo typical mechanical processing and release good mechanical behaviors, which is seldom observed in other COF materials [40].

Given these intriguing characters, the resulting compacted COF/CNT film composites were further processed into interdigital microelectrodes by using laser scribing (Fig. 4d) and then were assembled to the flexible planar all-solid-state MSCs on polyethylene terephthalate (PET) substrates (termed g-$C_{30}N_6$-COF-MSC and g-$C_{48}N_6$-COF-MSC) by using the ionogel electrolyte [1-ethyl-3-me thylimidazoliumtetrafluoroborate with poly(vinylidene fluoride-hexafluoropropylene) ($EMIMBF_4$/PVDF-HFP)] [19]. The COF/CNT microelectrodes displayed a valid area of ~2.0 cm^2 and an average thickness of ca. 10 μm (Fig. 4d). The retained cyclic voltammetry (CV) curves of both MSC devices at different scan rates of 5–5000 mV s^{-1} revealed their stable capacitive behavior and high electrochemical reversibility (Fig. 5a and b; Figs. S18 and S19 online). Significantly, MSC devices worked well at a large operating voltage of 2.5 V and withstood ultrahigh CV scan rates (up to 5000 mV s^{-1}), demonstrating the outstanding electrochemical activity and stability. The galvanostatic charge/discharge (GCD) profiles tested at different current densities revealed quasi-triangle in shape, further confirming the excellent capacitive behavior of these COF-based MSCs. Moreover, on the basis of the CV curves, the areal capacitances (C_A) of g-$C_{30}N_6$-COF-MSC were calculated as 44.3, 10.3, 6.6 and 2.3 mF cm^{-2} at scan rates of 5, 100, 500, and 5000 mV s^{-1}, respectively. Under the same scan

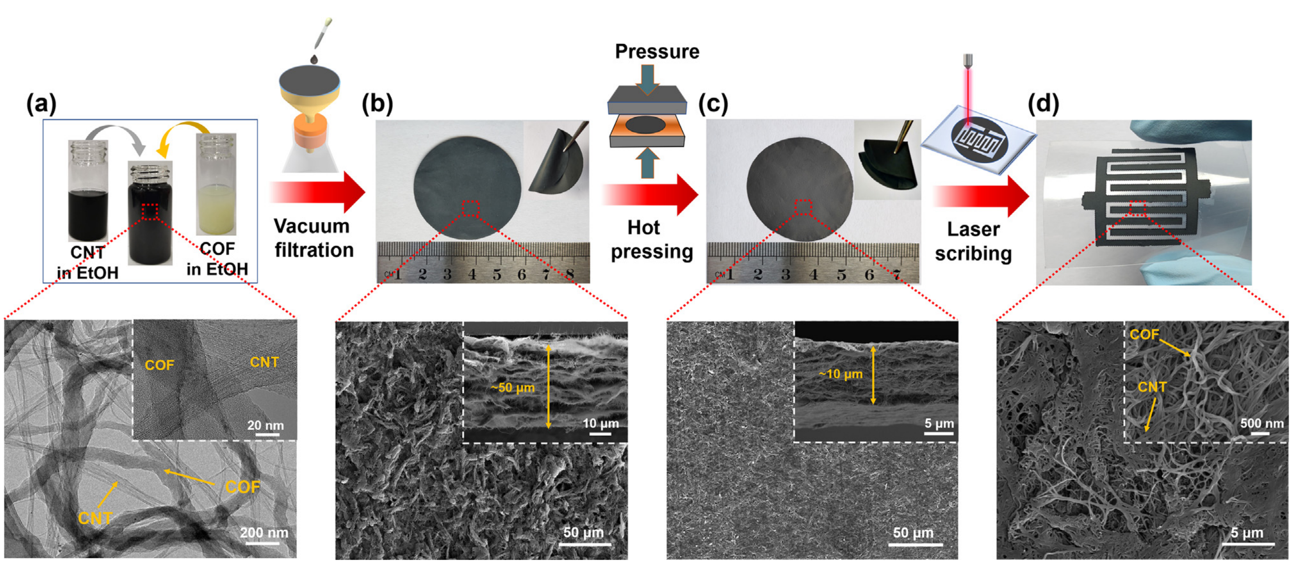

Fig. 4. (Color online) Process of the fabrication of COF-MSCs. (a) COF/CNT dispersion in ethanol (EtOH). Below: TEM image of COF/CNT dispersion (inset: magnified TEM image). (b) Photograph of as-prepared COF/CNT film. Below: top-view SEM image of the film (inset: side-view SEM image). (c) Photograph of COF/CNT film after hot-pressing treatment. Below: top-view SEM image of the film after hot-pressed treatment (inset: side-view SEM image). (d) Photograph of the as-fabricated COF-MSC electrodes on a flexible PET substrate. Below: top-view SEM image of COF-MSC electrodes (inset: magnified SEM image).

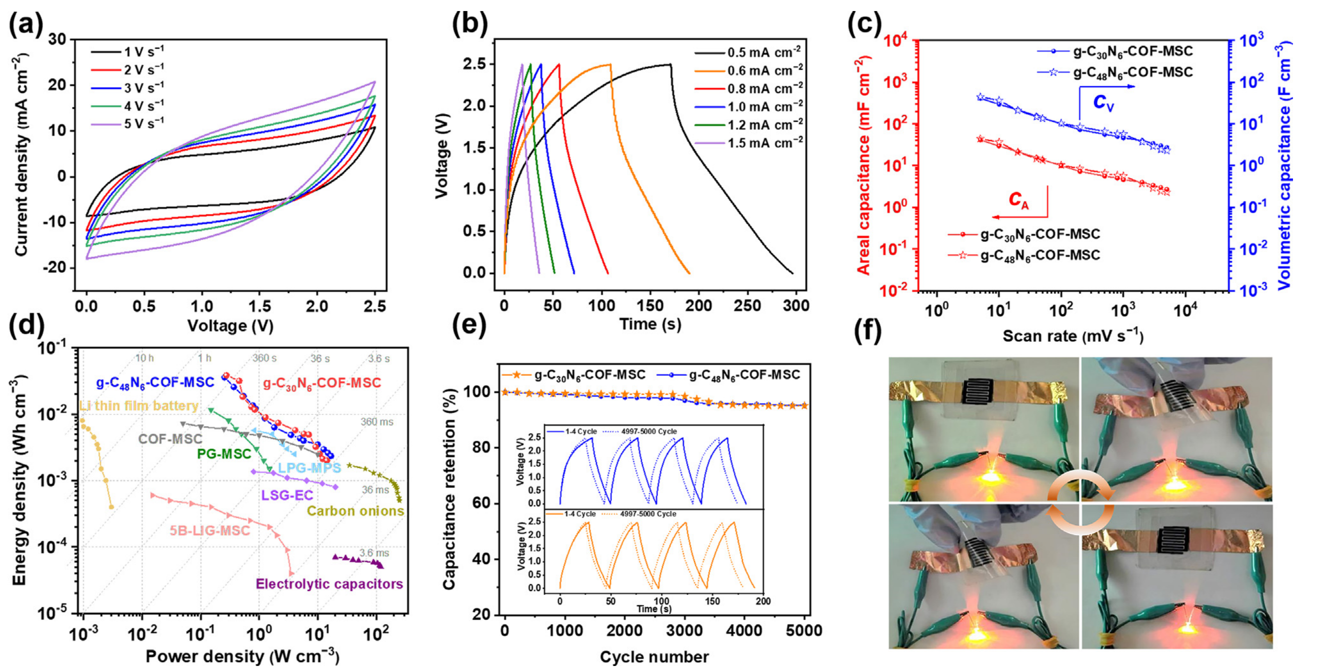

Fig. 5. (Color online) Electrochemical properties of COF-MSCs. (a) CV curves of g-$C_{30}N_6$-COF-MSC at scan rates from 1000 to 5000 mV s^{-1}. (b) GCD curves of g-$C_{30}N_6$-COF-MSC at current densities from 0.5 to 1.5 mA cm^{-2}. (c) The specific areal and volumetric capacitances (C_A and C_V) of g-$C_{30}N_6$-COF-MSC and g-$C_{48}N_6$-COF-MSC at different scan rates. (d) Ragone plot compared with commercially available electrochemical energy storage devices and some reported MSCs. (e) Cycling stability of g-$C_{30}N_6$-COF-MSC and g-$C_{48}N_6$-COF-MSC measured at 1.2 mA cm^{-2} under the voltage window of 2.5 V (inset shows the first four cycles and the last four cycles GCD curves). (f) Photographs of g-$C_{30}N_6$-COF-MSC powering a red LED with flatting and bending cycles.

rates, g-$C_{48}N_6$-COF-MSC offered the C_A of 41.1, 10.0, 5.6 and 2.7 mF cm^{-2}, respectively (Fig. 5c). The highest C_A values of the two COF-based MSCs were much higher than most of the reported MSCs (Table S4 online), such as phosphorene/graphene (9.8 mF cm^{-2}) [41], onion-like carbon (1.7 mF cm^{-2}) [42], LSG-MSC (laser-scribed graphene) (14.7 mF cm^{-2}) [43] and 5B-LIG-MSC (boron-doped laser-induced graphene) (16.5 mF cm^{-2}) [44]. The volumetric energy density and volumetric power density of the two COF-MSCs devices were calculated as shown in the Ragone plots (Fig. 5d). And g-$C_{30}N_6$-COF-MSC delivered volumetric energy densities of 38.5, 8.9, 5.7, and 2.0 mWh cm^{-3} at power densities of 0.3, 1.3, 4.1 and 14.4 W cm^{-3}, respectively, g-$C_{48}N_6$-COF-MSC exhibited volumetric energy densities of 35.7, 8.7, 4.9, and 2.3 mWh cm^{-3} at power densities of 0.3, 1.3, 3.5 and 16.9 W cm^{-3}, respectively. The maximum volumetric energy densities of the two as-prepared COF-MSCs (38.5 and 35.7 mWh cm^{-3}) were remarkably higher than those of commercially available energy storage devices, such as $\leq$ 10 mWh cm^{-3} for lithium thin-film batteries [45], 1.6 mWh cm^{-3} for onion-like carbon [42], 11.6 mWh cm^{-3} for phosphorene/graphene [41], 4 mWh cm^{-3} for LWG-MSCs (laser-written graphene) [46] and 7.3 mWh cm^{-3} for g-$C_{34}N_6$-COF-MSC [16], respectively (Table S4 online). Moreover, both COF-MSCs exhibit good cycling stability with almost 95% capacitance retention after 5000 charge/discharge cycles (Fig. 5e). Furthermore, as a proof of concept, one g-$C_{30}N_6$-COF-MSC device can power a 2.0 V red LED for at least 30 s under flatting and bending cycles, demonstrating its superior flexibility, high energy density and promising integration capability (Fig. 5f). In addition, COF-MSCs could be connected in series or parallel to increase the working voltage and capacitance output, respectively (Figs. S23 and S24 online). Obviously, the CV curves at 100 mV s^{-1} presented a sufficient voltage extension from 2.5 V for a single device to 5.0 V for two tandem devices (Figs. S23a and S24a online). Meanwhile, the two parallel devices provided almost twice the capacitance of a single device. According to the GCD curves at 1 mA cm^{-2} (Figs. S23b and S24b online), the two serially connected COF-MSCs also exhibited almost twice the output voltage of a single device, and the two devices in parallel exhibited a discharge time twice that of a single device, suggesting the superior capability of modular integration for these COF-MSCs. For comparison, the capacitance of a pure CNT-based MSC was only approximately 25% of the COF-MSCs, manifesting the pronounced contribution of COFs for the supercapacitive performance of the device (Fig. S25 and Table S3 online). The Nyquist plots further demonstrated the fast charge transfer rate and ionic diffusion in the as-prepared COF-MSCs (Fig. S28 online). The high capacitance and rate capability of COF-based MSCs were attributed to the synergistic effect of the composition of COF and CNT. Firstly, the nitrogen-enriched triazine groups in the COF networks offer abundant active sites over the open channels to enhance the supercapacitive performance of the devices [47]. Secondly, the hierarchical porous structures from nano- to micro-meter levels of the as-prepared COF/CNT hybrid films can considerably improve the ions transportation kinetics between the electrolyte and electrode materials, thus enhancing overall capacitance. Thirdly, the well-defined nanofibers of these COFs are uniformly interwoven with CNTs, essentially avoiding the restacking of CNTs or COF fibers. Thus, the accessible surface area is maintained, which guarantees ion diffusion at high operating speeds. Fourthly, the π-electron cloud stacking between CNTs and aromatic structures in these COFs may facilitate the electron transfer, leading to a high rate capability. Eventually, the high stability of the olefin-linked COFs and the unique properties of the ionogel electrolyte (such as excellent stability, nonvolatility and wide electrochemical window) all contribute to the high electrochemical performance of the as-fabricated MSC devices [19].

4. Discussion and conclusion

In conclusion, two new olefin-linked 2D COFs were synthesized by using 2,4,6-trimethyl-1,3,5-triazine and the tritopic triazine-cored aldehydes through Knoevenagel condensation. Both COFs possess highly crystalline honeycomb-like structures and abundant regular open nanochannels. Their well-defined morphologies of ultralong nanofibers were revealed. Such COF fibers were readily assembled with CNT to form free-standing COF/CNT thin films with excellent mechanical processability, allowing for further fabrication into interdigital electrodes for MSCs. By using the ionogel electrolyte of $EMIMBF_4$/PVDF-HFP, such COF-based MSCs delivered high areal capacitances, large operating voltage output, high volumetric energy densities and excellent cyclability. From this work, one can reasonably foresee that olefin-linked COFs could be regarded as a new type of polymers with well-defined topological structures and intriguing characteristics, which are valuable for fundamental research and practical application in the field of polymeric materials, nano-soft materials and semiconducting materials.

Conflict of interest

The authors declare that they have no conflict of interest.

Acknowledgments

The authors thank the National Natural Science Foundation of China (21774072, and 21720102002). This work was also financially supported by the Open Project Programs of the State Key Laboratory of Inorganic Synthesis and Preparative Chemistry (2019-01, Jilin University) and the State Key Laboratory for Modification of Chemical Fibers and Polymer Materials (KF2019, Donghua University). The authors also thank Xiaomin Li, Xinqiu Guo, Qunli Rao, Yan Li and Jie Zhang in the Instrumental Analysis Center of SJTU for their help on the SEM, TEM, PXRD, TGA and nitrogen physisorption measurements.

Author contributions

Fan Zhang and Shuai Bi (the corresponding authors) conceived the idea, designed the experiments and co-wrote the manuscript. Fan Zhang (the first author) implemented the whole project including synthesis and characterization of the COFs, device fabrication, data collection and manuscript writing. Shice Wei assisted the synthesis of COFs. Weiwei Wei, Jiang Zou, Guoying Gu and Dongqing Wu gave assistance in the preparation of micro-supercapacitor and analysis of electrochemical data. All the authors discussed the results and contributed to the accomplishment of the manuscript.

Appendix A. Supplementary materials

Supplementary materials to this article can be found online at https://doi.org/10.1016/j.scib.2020.05.033.

References

[1] Côté AP, Benin AI, Ockwig NW, et al. Porous, crystalline, covalent organic frameworks. Science 2005;310:1166–70.
[2] Lyu H, Diercks CS, Zhu C, et al. Porous crystalline olefin-linked covalent organic frameworks. J Am Chem Soc 2019;141:6848–52.
[3] Acharjya A, Pachfule P, Roeser J, et al. Vinylene-linked covalent organic frameworks by base-catalyzed aldol condensation. Angew Chem Int Ed 2019;58:14865–70.
[4] Jadhav T, Fang Y, Patterson W, et al. 2D poly(arylene vinylene) covalent organic frameworks via aldol condensation of trimethyltriazine. Angew Chem Int Ed 2019;58:13753–7.
[5] Wei S, Zhang F, Zhang W, et al. Semiconducting 2D triazine-cored covalent organic frameworks with unsubstituted olefin linkages. J Am Chem Soc 2019;141:14272–9.
[6] Zhuang X, Zhao W, Zhang F, et al. A two-dimensional conjugated polymer framework with fully sp^2-bonded carbon skeleton. Polym Chem 2016;7:4176–81.
[7] Jin E, Asada M, Xu Q, et al. Two-dimensional sp^2 carbon–conjugated covalent organic frameworks. Science 2017;357:673–6.
[8] Jin E, Li J, Geng K, et al. Designed synthesis of stable light-emitting two-dimensional sp^2 carbon-conjugated covalent organic frameworks. Nat Commun 2018;9:4143.
[9] Xu S, Wang G, Biswal BP, et al. A nitrogen-rich 2D sp^2-carbon-linked conjugated polymer framework as a high-performance cathode for lithium-ion batteries. Angew Chem Int Ed 2019;58:849–53.
[10] Zhao Y, Liu H, Wu C, et al. Fully conjugated two-dimensional sp^2-carbon covalent organic frameworks as artificial photosystem I with high efficiency. Angew Chem Int Ed 2019;58:5376–81.
[11] Chen R, Shi J-L, Ma Y, et al. Designed synthesis of a 2D porphyrin-based sp^2 carbon-conjugated covalent organic framework for heterogeneous photocatalysis. Angew Chem Int Ed 2019;58:6430–4.
[12] Becker D, Biswal BP, Kaleńczuk P, et al. Fully sp^2-carbon-linked crystalline two-dimensional conjugated polymers: insight into 2D poly (phenylenecyanovinylene) formation and its optoelectronic properties. Chem Eur J 2019;25:6562–8.
[13] Jin E, Lan Z, Jiang Q, et al. 2D sp^2 carbon-conjugated covalent organic frameworks for photocatalytic hydrogen production from water. Chem 2019;5:1632–47.
[14] Bi S, Yang C, Zhang W, et al. Two-dimensional semiconducting covalent organic frameworks via condensation at arylmethyl carbon atoms. Nat Commun 2019;10:2467.
[15] Bi S, Lan Z-A, Paasch S, et al. Substantial cyano-substituted fully sp^2-carbon-linked framework: metal-free approach and visible-light-driven hydrogen evolution. Adv Funct Mater 2017;27:1703146.
[16] Xu J, He Y, Bi S, et al. An olefin-linked covalent organic framework as a flexible thin-film electrode for a high-performance micro-supercapacitor. Angew Chem Int Ed 2019;58:12065–9.
[17] Zheng S, Shi X, Das P, et al. The road towards planar microbatteries and micro-supercapacitors: from 2D to 3D device geometries. Adv Mater 2019;31:1900583.
[18] Zhang P, Wang F, Yu M, et al. Two-dimensional materials for miniaturized energy storage devices: from individual devices to smart integrated systems. Chem Soc Rev 2018;47:7426–51.
[19] Zhou F, Huang H, Xiao C, et al. Electrochemically scalable production of fluorine-modified graphene for flexible and high-energy ionogel-based microsupercapacitors. J Am Chem Soc 2018;140:8198–205.
[20] Wu Z-S, Tan Y-Z, Zheng S, et al. Bottom-up fabrication of sulfur-doped graphene films derived from sulfur-annulated nanographene for ultrahigh volumetric capacitance micro-supercapacitors. J Am Chem Soc 2017;139:4506–12.
[21] Lin J, Peng Z, Liu Y, et al. Laser-induced porous graphene films from commercial polymers. Nat Commun 2014;5:5714.
[22] El-Kady MF, Ihns M, Li M, et al. Engineering three-dimensional hybrid supercapacitors and microsupercapacitors for high-performance integrated energy storage. Proc Natl Acad Sci USA 2015;112:4233.
[23] Wen L, Li F, Cheng H-M. Carbon nanotubes and graphene for flexible electrochemical energy storage: from materials to devices. Adv Mater 2016;28:4306–37.
[24] Hu M, Cui C, Shi C, et al. High-energy-density hydrogen-ion-rocking-chair hybrid supercapacitors based on $Ti_3C_2T_x$ MXene and carbon nanotubes mediated by redox active molecule. ACS Nano 2019;13:6899–905.
[25] Kurra N, Ahmed B, Gogotsi Y, et al. Mxene-on-paper coplanar microsupercapacitors. Adv Energy Mater 2016;6:1601372.
[26] Li H, Hou Y, Wang F, et al. Flexible all-solid-state supercapacitors with high volumetric capacitances boosted by solution processable mxene and electrochemically exfoliated graphene. Adv Energy Mater 2017;7:1601847.
[27] Zhang C, Kremer MP, Seral-Ascaso A, et al. Stamping of flexible, coplanar micro-supercapacitors using mxene inks. Adv Funct Mater 2018;28:1705506.
[28] Li J, Shi Q, Shao Y, et al. Cladding nanostructured AgNWs-MoS_2 electrode material for high-rate and long-life transparent in-plane micro-supercapacitor. Energy Storage Mater 2019;16:212–9.
[29] Yang W, He L, Tian X, et al. Carbon-mems-based alternating stacked MoS_2@rGO-CNT micro-supercapacitor with high capacitance and energy density. Small 2017;13:1700639.
[30] Halder A, Kandambeth S, Biswal BP, et al. Decoding the morphological diversity in two dimensional crystalline porous polymers by core planarity modulation. Angew Chem Int Ed 2016;55:7806–10.
[31] Wang K, Yang L-M, Wang X, et al. Covalent triazine frameworks via a low-temperature polycondensation approach. Angew Chem Int Ed 2017;56:14149–53.
[32] Liu M, Huang Q, Wang S, et al. Crystalline covalent triazine frameworks by in situ oxidation of alcohols to aldehyde monomers. Angew Chem Int Ed 2018;57:11968–72.
[33] Liu M, Jiang K, Ding X, et al. Controlling monomer feeding rate to achieve highly crystalline covalent triazine frameworks. Adv Mater 2019;31:1807865.
[34] Liu J, Zan W, Li K, et al. Solution synthesis of semiconducting two-dimensional polymer via trimerization of carbonitrile. J Am Chem Soc 2017;139:11666–9.
[35] Liu J, Lyu P, Zhang Y, et al. New layered triazine framework/exfoliated 2D polymer with superior sodium-storage properties. Adv Mater 2018;30:1705401.
[36] Kuhn P, Antonietti M, Thomas A. Porous, covalent triazine-based frameworks prepared by ionothermal synthesis. Angew Chem Int Ed 2008;47:3450–3.

[37] Ren S, Bojdys MJ, Dawson R, et al. Porous, fluorescent, covalent triazine-based frameworks via room-temperature and microwave-assisted synthesis. Adv Mater 2012;24:2357–61.
[38] Wang S, Zhang Z, Zhang H, et al. Reversible polycondensation-termination growth of covalent-organic-framework spheres, fibers, and films. Matter 2019;1:1592–605.
[39] Vyas VS, Haase F, Stegbauer L, et al. A tunable azine covalent organic framework platform for visible light-induced hydrogen generation. Nat Commun 2015;6:8508.
[40] Halder A, Ghosh M, Khayum MA, et al. Interlayer hydrogen-bonded covalent organic frameworks as high-performance supercapacitors. J Am Chem Soc 2018;140:10941–5.
[41] Xiao H, Wu Z-S, Chen L, et al. One-step device fabrication of phosphorene and graphene interdigital micro-supercapacitors with high energy density. ACS Nano 2017;11:7284–92.
[42] Pech D, Brunet M, Durou H, et al. Ultrahigh-power micrometre-sized supercapacitors based on onion-like carbon. Nat Nanotechnol 2010;5:651–4.
[43] El-Kady MF, Kaner RB. Scalable fabrication of high-power graphene micro-supercapacitors for flexible and on-chip energy storage. Nat Commun 2013;4:1475.
[44] Peng Z, Ye R, Mann JA, et al. Flexible boron-doped laser-induced graphene microsupercapacitors. ACS Nano 2015;9:5868–75.
[45] Wu Z-S, Parvez K, Winter A, et al. Layer-by-layer assembled heteroatom-doped graphene films with ultrahigh volumetric capacitance and rate capability for micro-supercapacitors. Adv Mater 2014;26:4552–8.
[46] Gao W, Singh N, Song L, et al. Direct laser writing of micro-supercapacitors on hydrated graphite oxide films. Nat Nanotechnol 2011;6:496–500.
[47] Hao L, Ning J, Luo B, et al. Structural evolution of 2D microporous covalent triazine-based framework toward the study of high-performance supercapacitors. J Am Chem Soc 2015;137:219–25.

Fan Zhang received her B.S. degree in Chemistry from Shandong Normal University in 2018. At present, she is a graduate student of School of Chemistry and Chemical Engineering of Shanghai Jiao Tong University. She focuses on conjugated covalent organic frameworks for energy conversion and storage.

Shuai Bi is currently a postdoctoral fellow in Shanghai Jiao Tong University (2020–present). He received his bachelor degree in 2014 and Ph.D. degree in 2019 from Shanghai Jiao Tong University. His research interest is mainly focused on the development of 2D conjugated covalent organic frameworks for energy and environmental science.

Fan Zhang received his B.E. degree in Electrochemistry from Shanghai Jiao Tong University in 1991, and his Ph.D. degree in Organic Chemistry from Jilin University in 2000. After more than eight years of research experience in Germany and United States, he was promoted to a full Professor at School of Chemistry and Chemical Engineering of Shanghai Jiao Tong University, China. His research interests span from organometallic catalysis and polymerization methodology to organic π-conjugated functional materials for energy conversion and storage.